International Journal of Coal Geology 224 (2020) 103483

Contents lists available at ScienceDirect

International Journal of Coal Geology

journal homepage: www.elsevier.com/locate/coal

# The structural versus textural control on the methane sorption capacity of clay minerals

Paweł P. Ziemiański[a,*], Arkadiusz Derkowski[a,*], Jakub Szczurowski[b], Marcin Kozieł[c]

[a] Institute of Geological Sciences, Polish Academy of Sciences, Senacka 1, PL-31002 Kraków, Poland
[b] Faculty of Energy and Fuels, AGH University of Science and Technology, Mickiewicza 30, PL-30059 Kraków, Poland
[c] Faculty of Chemistry, Jagiellonian University, Gronostajowa 2, PL-30387 Kraków, Poland

ARTICLE INFO

*Keywords:*
High-pressure adsorption
Methane
Carbon dioxide
Nitrogen
Shale gas
Smectite

ABSTRACT

In the natural, high-pressure environments of sediments and sedimentary rocks, clay minerals, along with organic matter, contribute to a large portion of the available surface area and microporosity in which methane ($CH_4$) can be adsorbed. However, most of the questions concerning the location of adsorption sites, e.g. interlayer accessibility for $CH_4$, remain unknown. Here, we have separately investigated the textural and structural control on $CH_4$ high-pressure adsorption on pure clay minerals by combining high- and low-pressure gas adsorption techniques, transmission electron microscopy, and thermogravimetric and X-ray diffraction analyses on various cationic forms of montmorillonite, beidellite, and two illites, with different contents of adsorbed water. The results show that $CH_4$ adsorption capacity is controlled by $N_2$-accesible micropore volume. $CH_4$ adsorption sites are located mainly outside of the interlayer galleries unless they are open wide enough (e.g. pillared by organic cations or incompletely dried divalent cations). However, the structure-independent factors like the crystallite planar dimensions and the way that they assemble are the main control on $CH_4$ adsorption capacity. This might be the reason for the inconsistencies in $CH_4$ adsorption reported for clay minerals in the literature. $CO_2$ adsorption measurements, assumed to provide a good proxy for the estimation of $CH_4$ adsorption capacity in natural mudrocks, may overestimate the $CH_4$ adsorption potential in geomaterials containing a significant amount of exchangeable divalent cations due to higher penetrability of $CO_2$ than $CH_4$ in the interlayers of expandable clay minerals.

## 1. Introduction

The majority of methane ($CH_4$) present on Earth occurs in high-pressure environments, such as $CH_4$ clathrates in oceanic bottom sediments (Kvenvolden, 1998), and in sedimentary rocks: coalbeds and various types of hydrocarbon reservoirs, including clay-rich mudrocks and shales (Rexer et al., 2013; Ross and Bustin, 2009; Topór et al., 2017a, 2017b; Zee Ma, 2016). Due to the high pressure in geological formations, a significant amount of $CH_4$ can be adsorbed physically on surfaces and in micro- and mesopores of sediments and sedimentary rocks. These textural features are commonly suggested to be controlled by two compounds: organic matter and clay minerals (Kuila et al., 2014; Topór et al., 2017b). Among clay minerals, illite, smectite, and their interstratified variety (mixed-layered illite-smectite mineral) are the most abundant and widespread mineral types in Earth's upper crust (Garrels and Mackenzie, 1971), and are present in the all above-mentioned sedimentary environments. Illite and smectite are formed by the 2:1 layers consisting of an octahedral sheet sandwiched between two tetrahedral sheets. The major difference between these two species is in the interlayer occurring between the 2:1 layers. It has a fixed width of ~0.3 nm and is filled by potassium, in case of micas (e.g. illite), whereas the interlayer cations in smectite are in a hydrated form and can be exchanged by any cation, organic or inorganic, present in the environment. The type of exchangeable cation and its hydration properties determine the smectite interlayer width, thus its expandability at a given hydration state and therefore controls gas accessibility in the interlayer (see Bowers et al., 2017, 2018; Lee et al., 2018; Loganathan et al., 2018).

Whereas the control of sedimentary organic matter (kerogen, solid bitumen) on $CH_4$ adsorption has been investigated intensively (Rexer et al., 2014; Topór et al., 2017b; Zee Ma, 2016), the mechanism of clay minerals – $CH_4$ interactions has been a subject of only a few studies, which focused on differences in adsorption capacity in the different clay species. The most intriguing question is whether the expandable clay

* Corresponding authors.
*E-mail addresses:* ndziemia@cyf-kr.edu.pl (P.P. Ziemiański), ndderkow@cyf-kr.edu.pl (A. Derkowski).

https://doi.org/10.1016/j.coal.2020.103483
Received 18 December 2019; Received in revised form 11 April 2020; Accepted 12 April 2020
Available online 13 April 2020

minerals (smectite, illite-smectite) can adsorb methane in the interlayer, which would increase their methane adsorption capacity to a range proportional to their expandable component. Experimental investigation of $CH_4$ intercalation in expandable clay minerals under water-saturated conditions showed a formation of clay-methane clathrates in the interlayer galleries (Guggenheim and Koster van Groos, 2003). Water content, however, may not always be present in the environment in quantities that allow clathrates formation.

Liu et al. (2013) postulated that $CH_4$ molecules are able to enter the interlayer space of expandable clays minerals even after prior drying at 200 °C. Basal spacing > 1.15 nm that – according to Bowers et al. (2018) - allows methane intercalation, corresponds to the interlayer width ~ 0.40 nm. Such a spacing requires the presence of tightly-bound water molecules ($H_2O$) coordinated directly to interlayer cations, forming a part of the first hydration shell (Ferrage et al., 2007a, 2007b; Kuligiewicz and Derkowski, 2017). Using the ab initio molecular dynamic model of $CH_4$ adsorption in Ca-montmorillonite under 120 bar, Lee et al. (2018) suggested a ~ 10% expansion of basal spacing after $CH_4$ intercalation when interlayer $Ca^{2+}$ was hydrated with 2–3 molecules of $H_2O$. Methane interlayer intercalation under such conditions also distorted tetrahedral symmetry of $CH_4$ which induced relatively large dipole moments in the $CH_4$ molecules, increasing their adsorption ability. However, due to the high affinity of $H_2O$ to the exchangeable cations present in the clay mineral's interlayers, $H_2O$ adsorbs in the interlayer at the expense of $CH_4$ when the relative humidity of methane gas increases (Bowers et al., 2018; Li et al., 2016; Rao et al., 2013; Rao and Leng, 2014). Additionally, capillary water present in humid conditions reduce the available surface area for $CH_4$ adsorption by blocking pore space (Li et al., 2016).

Methane adsorption capacity measured on pure or almost pure clay mineral samples return highly variable results, depending on the pretreatment and measurement conditions, and the actual state and form of a sample (cf. Ji et al., 2012; Li et al., 2016; Liu et al., 2013). For example, maximum excess methane adsorption measured on illite varies from 0.055 mmol/g (35 °C; Liang et al., 2016) to 0.13 mmol/g (30 °C; Ross and Bustin, 2009). In turn, Ji et al. (2012) found that in some phyllosilicate minerals (chlorite) adsorption capacity strongly depends on the grain size, while for the others (montmorillonite) differences are insignificant. Those authors presented a linear relationship between specific surface area measured with subcritical $N_2$ gas adsorption and the high-pressure $CH_4$ adsorption capacity. That relationship suggests textural control on methane adsorption on clay minerals, as $N_2$ at −196 °C is mainly adsorbed on the basal planes of smectite crystallites and in the meso- and micropores formed due to irregular stacking of the clay mineral layers (Kaufhold et al., 2010; and references therein), with microporosity located mainly at the edges of the crystallites (Michot and Villiéras, 2006).

Methane adsorption studies performed so far on pure, or apparently pure clay minerals, present inconsistent results; the actual location of the adsorption sites in a clay sample, and nature of texture that are controlling high-pressure $CH_4$ adsorption are still confusing. The main aim of the present study is to understand whether the main control of $CH_4$ adsorption on clay minerals originates from textural, structure-independent factors (i.e. grain sizes, the way crystallites assemble), or whether it primarily comes from their crystal-chemical structure.

## 2. Materials

The high-charge montmorillonite (Mtm) (SAz-1 “Cheto” Apache Country, Arizona) and low-charge beidellite (BId) SBId-1 (Glen Silver Pit, DeLamare Mine, Idaho) obtained from The Clay Minerals Society Source Material Repository were used in the present study representing different expandable 2:1 layer type clay minerals, with a different layer charge location. The chemical formulas of the Mtm and BId are: $M^{+}_{0.57}[(Al_{1.40}Fe^{3+}_{0.10}Mg_{0.50})(Si_{3.93}Al_{0.07})O_{10}(OH)_2]$ (Jaynes and Bigham, 1987), and $M^{+}_{0.34}[(Al_{1.89}Fe^{3+}_{0.06}Mg_{0.11})(Si_{3.64}Al_{0.37})O_{10}(OH)_2]$ (Post et al., 1997), respectively.

Two illitic materials were selected to represent the 2:1 layer type of non-expandable clay minerals; hydrothermal Zempleni illite (marked as Zempleni), from Füzérradvány, Hungary (Viczián, 1997), with an average of 17% of smectite layers (Veblen et al., 1990) and an ultra-fine-grained, barrel-shape illite of lacustrine origin from Le Puy, France (marked as LePUY), with less than 20% of smectite layers (Rajec et al., 1999).

Two samples of high-surface adsorbents were used as a reference material for high-pressure adsorption experiments: commercial activated carbon WS-480 (marked as AC WS480), produced by Calgon Carbon Corporation (Munusamy et al., 2011), and 5A zeolite (marked as Zeolite 5A; Quantachrome reference material # 2012).

### 2.1. Preparation

#### 2.1.1. Standard samples

Due to sufficient purity, (> 90% of the clay phase in a sample) Mtm and Zempleni samples were used as as-shipped material, and were not purified or fractionated, if not specifically stated otherwise in this paper. Due to significant content of impurities, LePUY and BId samples underwent purification by removing carbonates, organic matter, and Fe-oxides/hydroxides by a sequential treatment in buffered acetic acid, sodium hypochlorite, and buffered sodium dithionite (Jackson, 1969). Grain size fractions of < 2 μm for BId, and < 0.02 μm for LePUY were separated by centrifugation of a clay suspension with a regular centrifuge (fraction < 2 μm: 1000 rpm, 4 min, 1 $dm^3$ holder in S70 Janetzki) and through-flow ultracentrifuge (fraction < 0.02 μm; 8000 rpm, 3.9 cc/min of 0.5 g/$dm^3$ sample suspension, Beckman J2-MC centrifuge), cleaned by dialysis and dried at 60 °C.

Smectites underwent interlayer cation exchange for $Mg^{2+}$, $Ca^{2+}$, $Li^{+}$, $Cs^{+}$, $Na^{+}$, and tetramethylammonium ($TMA^{+}$), by dispersing the powdered sample in one-normal solution of a corresponding salt (chloride) with a cation concentration > 10 times (> 20 times for Na- and Li- forms; Steudel and Emmerich, 2013) of the sample's cation exchange capacity. Suspensions were shaken for 1 h and centrifuged (7000 RPM, 30 min), to remove the supernatant solution. The procedure was repeated four times. Excess electrolytes were removed by dialysis. The samples were dried at 60 °C. Clay flakes formed after drying were carefully crushed in a hand mortar.

#### 2.1.2. Oriented and disoriented samples

Disoriented and highly oriented specimens were prepared from the < 2 μm grain fraction of Na-exchanged Mtm purified and separated as above (Jackson, 1969). The fraction was split in two homogenous and representative portions. One portion (~0.7 g) was dispersed in 18 cc of deionized water and transferred onto a glass slide surface to air dry (glass slide method). The dry sample film was then carefully removed from the glass using a razorblade. The disoriented specimen was prepared by a freeze-drying method using the other portion of the sample dispersed in deionized water to 0.45 wt% suspension. The suspension was frozen at −42 °C and kept under vacuum (< 0.133 mbar) at −49 °C, until the water was removed, using the Labconco® FreeZone and Shell Freezer devices.

## 3. Experimental

### 3.1. High-pressure methane sorption

The supercritical, high-pressure experiments were conducted using an IsoSORP® gravimetric sorption analyzer, provided by Rubotherm (Germany). The detailed description of the device and its working principle has been reported elsewhere (Dreisbach and Lösch, 2000). The device allows in situ drying of the samples before analysis without exposing them to laboratory environment. Also, it allows simultaneous determination of bulk gas density during adsorption experiments, in

order to avoid any uncertainly related to the equation of gas state.

At least 0.6 g of each sample was mounted in the adsorption chamber and subsequently dried in situ at 60, 110, and 210 °C in vacuum (~1 Pa) for 20 h, to remove portions of the clay bound water (cf. Kuligiewicz and Derkowski, 2017). Only the masses of highly oriented and disoriented Na-exchanged Mtm samples were lower (0.2 g), due to the very low bulk density of the freeze-dried sample ("cotton-like" texture). Additionally, one portion of the TMA-exchanged Mtm sample was pre-dried ex situ at 315 °C for 20 h and then dried in the IsoSORP® at 210 °C for 4 h before analysis. Zeolite 5A and activated carbon WS-480 were dried in-situ at 210 and 160 °C, respectively, until a stable mass was observed (at least 4 h).

Each in-situ drying step was followed by the determination of the sample's volume and mass, by measuring its buoyancy in helium (> 99.999% purity, Air Products, Poland). The grain volume measurement was followed by determination of the adsorption and desorption isotherms of $CH_4$ (> 99.9995% purity, obtained from Air Liquid, Poland) from zero to 150 bar (at least 16 adsorption and 12 desorption data points), at 25 °C. Each adsorption/desorption step lasted 60 min, which allowed equilibration of both temperature and pressure and enabled the sample to reach a stable mass (corresponding to roughly < 0.002 mmol/g change over last 10 min of equilibration; see Supplementary Materials SP. 1). The excess adsorption isotherms were calculated by Rubotherm System Control Software® (Dreisbach et al., 2002).

The samples and results of $CH_4$ adsorption are presented as followings: "Cation abbreviation" _ "sample name" _ "drying temperature in °C" "Cpt". (f) is added to each sample name, whenever a grain size fraction instead of a bulk sample was used. "Orient_" and "Disorient_" are added to Na_Mtm(f) < 2 um fraction to denote oriented and disoriented specimens, respectively.

### 3.2. Low-pressure nitrogen and carbon dioxide adsorption

Subcritical gas adsorption isotherms were measured using AUTOSORB-1-C (Quantachrome Instruments, USA) apparatus. 0.3 g portion of each sample was degassed at 60, 110, or 210 °C for 20 h under high vacuum of ~0.001 Pa, prior to the analysis, to correspond to the heating conditions in the IsoSORP® device. The nitrogen ($N_2$) isotherms were collected at −196 °C up to an atmospheric pressure (pressure; p/pressure of condensation; $p^0 \sim 1$). The carbon dioxide ($CO_2$) isotherms were collected at 0 °C up to atmospheric pressure ($p/p^0 \sim 0.03$).

All texture parameters were calculated using Quantachrome AS1WIN software provided by Quantachrome™ (Anton Paar). Using $N_2$ adsorption isotherms, micropore volume was calculated using the Dubinin-Radushkevich (DR) equation ($V_{m\_DR\_N2}$; Chen and Yang, 1994), and with the t-plot method ($V_{m\_t\text{-}plot\_N2}$; Lippens and Boer, 1965), using the Harkins-Jura statistical thickness equation (de Boer et al., 1966; Harkins and Jura, 1944), based on $N_2$ adsorption on nonporous $Al_2O_3$. Specific surface area was calculated using Brunauer, Emmett and Teller theory (SSA BET; Brunauer et al., 1938) with fitting approach appropriate for microporous adsorbents, presented by Rouquerol et al. (2007). Due to SSA BET sensitivity for microporosity, the external surface area (ESA) has been calculated, by adjusting SSA BET with the previously described t-plot technique. Low-pressure $CO_2$ adsorption isotherms were used for calculations of micropore volume using the DR equation ($V_{m\_DR\_CO2}$; Chen and Yang, 1994).

### 3.3. Transmission electron microscopy

Sodium-exchanged Mtm(f), BId(f), LePUY(f), and Zempleni samples were dispersed in deionized water at 0.0025 wt% concentration in order to achieve full osmotic swelling of fundamental particles (Norrish, 1954). Two to three droplets of 32% ammonia solution were added to the suspensions to decrease water surface tension. Each suspension was subjected to ultrasonic treatment for 5 min at 10 W power. One droplet of each suspension was transferred to 300 mesh grids copper holder, covered with formvar film. Droplets were removed after 30 s from holders. The particle observation was performed using a JEOL JEM2100HT (Jeol Ltd., Japan) transmission electron microscope (TEM) operating under 80 kV accelerating voltage.

### 3.4. Thermogravimetric analysis

Thermogravimetric analyses (TG) were performed using TA Discovery apparatus (by TA Instruments, USA) under 50 cc/min flow of pure nitrogen (99.999%, by Air Products). 20 mg of each air-dry, cation-exchanged sample was loaded on high-temperature platinum holders. TG experiments were composed of multiple isothermal heating steps at 60, 110, and 210 °C (additional step at 315 °C for TMA_Mtm) for 16 h each, to reflect the drying protocol in the IsoSORP® apparatus. In order to obtain the fully dehydroxylated mass of a sample, the last isothermal steps were followed by ramp heating to 1000 °C with a 20 °C/min rate.

### 3.5. X-ray diffraction

Powder X-ray diffraction (XRD) experiments were performed on a PANalytical X'pert PRO MPD diffractometer equipped with the Anton Paar TTK-450 temperature chamber. The measurements were carried out in vacuum using Cu X-ray source ($\lambda K\alpha = 0.15418$ nm) in Bragg-Brentano geometry. The individual patterns (3–40° 2θ) were collected for 30 min each. After each isothermal heating, the final XRD pattern was obtained by averaging the last four scans, after 10 h of drying at the desired temperature (60, 110, 210, 315 °C). Isothermal runs were separated by the ramp-heating intervals with a 5 °C/min rate required to reach the following isothermal step.

## 4. Results

### 4.1. High-pressure methane sorption experiments

So-called "excess adsorption" is the only quantity that can be directly measured in adsorption experiments. For low-pressure experiments, excess adsorption corresponds to absolute adsorption. Under high-pressure, however, the excess adsorption does not represent the whole amount of adsorbate that is present in the adsorption phase (absolute adsorption), which can be calculated using assumptions about the adsorbate phase density or volume (Do and Do, 2003). Because the adsorbate's density and its particular location on the clay mineral surface is vague and may vary between the same, but differently conditioned sample, maximum excess adsorption ($n_{\_CH4\_max}$) was used in this study as the only quantitative value of $CH_4$ adsorption. Detailed models of the conversion between excess adsorption and absolute adsorption are given elsewhere (Do and Do, 2003, and references therein).

Three main groups of high-pressure $CH_4$ adsorption isotherms were distinguished and defined below based on the isotherms' characteristic features (Fig. 1). For the purpose of discussion, they are labelled hereafter as E-, H-, and L-type isotherm.

The TMA_Mtm $CH_4$ isotherms were the only members of the clay mineral isotherms labelled hereafter as "E-type" group (E; extreme adsorption, Fig. 1A), characterized by the lack of hysteresis and high maximum adsorption ($n_{\_CH4\_max}$; from 1.24 mmol/g after drying at 60 °C to 1.52 mmol/g after 315 °C treatment; Table 1), 2.5 to 5.0 times higher that recorded on other cation forms of Mtm. 5A zeolite ($n_{\_CH4\_max}$ 4.09 mmol/g) and WS480 activated carbon ($n_{\_CH4\_max}$ 6.20 mmol/g; Fig. 1I; Table 1) also returned the E-type isotherm. The shape of both TMA_Mtm and 5A zeolite isotherms showed rapid increase at low pressure and the adsorption maximum was reached at relatively low pressure (60–70 bar). Further drying of TMA_Mtm, at 210 and 315 °C (*ex situ*) consecutively increased $n_{\_CH4\_max}$ by ~10% and ~ 23% relative to that after drying at 110 °C, respectively (Fig. 1A).

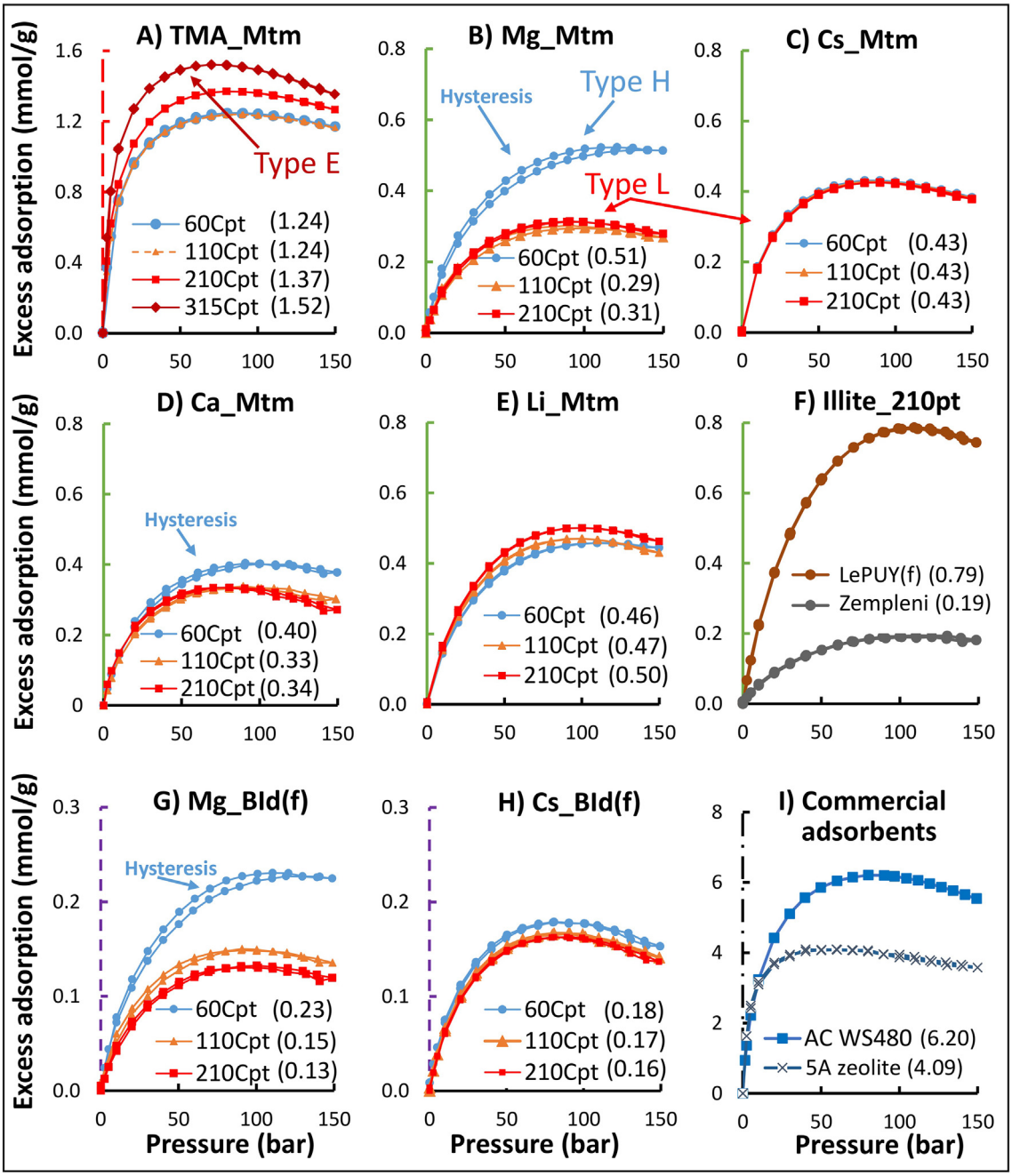


**Fig. 1.** High-pressure $CH_4$ adsorption isotherms on cation-exchanged montmorillonite (SAz-1), beidellite (SBId-1), illites (LePUY and Zempleni) and commercial gas adsorbents (activated carbon and 5A zeolite) after drying at a specified temperature. Maximum excess adsorption added in brackets (mmol/g). Note differences in y-axis scale.

The second type of methane adsorption isotherms were represented here by the Mg_Mtm_60Cpt (Fig. 1B) and labelled hereafter as "H-type" (H; hysteresis). All H-type isotherms reached their maximum points within a very high-pressure region (110–140 bar). H-type isotherms were characteristic for all other divalent cation-exchanged smectites, dried at 60 °C: Ca_Mtm_60Cpt (Fig. 1D), and Mg_BId(f)_60Cpt (Fig. 1G). Further drying at 110 °C of the samples showing H-type isotherm resulted in a significant decrease in $n_{CH4\_max}$ (from 0.51 mmol/g to 0.29 mmol/g for Mg_Mtm, 0.40 mmol/g to 0.33 mmol/g for Ca_Mtm, and 0.23 mmol/g to 0.15 mmol/g for Mg_BId(f); cf. Table 1, Fig. 1 B, D, G).

The isotherm of Mg_Mtm_210Cpt represents the "L-type" (L – low adsorption; Fig. 1B). The L-type isotherms showed no hysteresis, and relatively low $n_{CH4\_max}$ with respect to the E-type (from 0.13 mmol/g for Mg_BId(f)_210Cpt to 0.79 mmol/g for LePUY(f); Table 1). The isotherm shapes were distinctly different from the H-type; all L-type isotherms reached their maximum sorption at ~90 bar. Whenever a sample showed the H-type of isotherm, the L-type isotherms with lower adsorption maxima are obtained after drying at higher temperature. The L-type isotherm was observed for all the samples exchanged with a monovalent cation (Cs/Li_Mtm_60/110/210Cpt, Cs_BId(f)_60/110/210Cpt) and for the divalent cation-exchanged smectites dried at 110 °C or higher temperature (Mg/Ca_Mtm_110/210Cpt, Mg_BId(f)_110/210Cpt). Further drying, at a higher temperature, of the samples showing L-type of isotherms did not cause significant changes in the isotherms' shape, nor $n_{CH4\_max}$ (i.e. Mg_Mtm, Li_Mtm; Fig. 1B, E; Table 1), or did not change the isotherm at all (Cs_Mtm after any drying step; Fig. 1C). Mg_Mtm_110Cpt and Mg_BId(f)_110Cpt, however, even

**Table 1**
Maximum high-pressure excess adsorption of methane, specific surface area BET, external surface area, and $N_2$ and $CO_2$ microporosity for investigated samples.

| Sample name | $n_{CH4\_max}$ (mmol/g) | SSA BET ($m^2$/g) | ESA ($m^2$/g) | $V_{m\_DR\_N2}$ (cc/g) | $V_{m\_DR\_CO2}$ (cc/g) |
|---|---|---|---|---|---|
| Cs_Mtm_60Cpt | 0.43 | 58.8 | 29.3 | 0.021 | 0.094 |
| Cs_Mtm_110Cpt | 0.43 | 60.7 | 27.7 | 0.021 | 0.091 |
| Cs_Mtm_210Cpt | 0.43 | 71.9 | 31.2 | 0.025 | 0.089 |
| Mg_Mtm_60Cpt | 0.51 | 128.1 | 34.1 | 0.047 | 0.097 |
| Mg_Mtm_110Cpt | 0.29 | 63.2 | 31.4 | 0.023 | 0.032 |
| Mg_Mtm_210Cpt | 0.31 | 71.5 | 34.1 | 0.023 | 0.022 |
| TMA_Mtm_60Cpt | 1.24 | 180.8 | 28.0 | 0.065 | – |
| TMA_Mtm_110Cpt | 1.24 | 194.3 | 30.5 | 0.069 | – |
| TMA_Mtm_210Cpt | 1.37 | – | – | – | – |
| TMA_Mtm_315Cpt | 1.52 | 273.1 | 28.2 | 0.110 | 0.106 |
| Ca_Mtm_60Cpt | 0.40 | 55.1 | 29.8 | 0.020 | 0.056 |
| Ca_Mtm_110Cpt | 0.33 | 70.0 | 32.1 | 0.027 | 0.028 |
| Ca_Mtm_210Cpt | 0.34 | 85.5 | 33.2 | 0.033 | 0.026 |
| Li_Mtm_60Cpt | 0.46 | 64.3 | 38.0 | 0.026 | 0.037 |
| Li_Mtm_110Cpt | 0.47 | – | – | – | – |
| Li_Mtm_210Cpt | 0.50 | 117.6 | 46.1 | 0.032 | 0.025 |
| Disorient_Na_Mtm(f)_60Cpt | 0.37 | – | – | – | – |
| Disorient_Na_Mtm(f)_110Cpt | 0.38 | – | – | – | – |
| Disorient_Na_Mtm(f)_210Cpt | 0.38 | 58.4 | 12.8 | 0.023 | 0.030 |
| Orient_Na_Mtm(f)_60Cpt | 0.47 | – | – | – | – |
| Orient_Na_Mtm(f)_110Cpt | 0.47 | – | – | – | – |
| Orient_Na_Mtm(f)_210Cpt | 0.44 | 72.8 | 18.9 | 0.029 | 0.033 |
| Cs_BId(f)_60Cpt | 0.18 | – | – | – | – |
| Cs_BId(f)_110Cpt | 0.17 | – | – | – | – |
| Cs_BId(f)_210Cpt | 0.16 | 43.8 | 24.2 | 0.014 | 0.070 |
| Mg_BId(f)_60Cpt | 0.23 | 85.9 | 27.8 | 0.034 | 0.114 |
| Mg_BId(f)_110Cpt | 0.15 | – | – | – | – |
| Mg_BId(f)_210Cpt | 0.13 | 22.1 | 20.1 | 0.006 | 0.011 |
| Zempleni_210Cpt | 0.19 | 38.5 | 38.5 | 0.008 | 0.010 |
| LePUY(f)_210Cpt | 0.79 | 165.7 | 153.1 | 0.043 | 0.039 |

though classified as an example of the L-type isotherms, still showed residual hysteresis that disappeared after drying at 210 °C (Fig. 1B, G).

The $CH_4$ adsorption isotherms obtained from illitic samples is presented in Fig. 1F. No sign of hysteresis was observed. The shape of both, the Zempleni_210Cpt and LePUY_210Cpt isotherms corresponded to L-type. The $n_{CH4\_max}$ on LePUY(f)_210Cpt (0.79 mmol/g; Table 1) was ca. 4 times higher than Zempleni_210Cpt (0.19 mmol/g; Table 1).

$CH_4$ adsorption isotherms obtained on highly oriented and disoriented Na-Mtm(f) samples are presented in Fig. 2A, B, C. The maximum adsorption was ~25% higher for Orient_Na_Mtm(f) than for the Disorient_Na_Mtm(f) when dried at 60 °C and ca. 10% higher after drying at 210 °C (Table 1). All the Na-exchanged isotherms were of the L-type.

$CH_4$ adsorption reproducibility was tested on different batches of Mg-exchanged Mtm chosen as the material most sensitive to hydration, interlayer accessibility, and predrying conditions. The $CH_4$ isotherms of separately prepared batches fully overlap, whereas long rehydration under humid conditions caused only a minor shift of the isotherm of the sample predried at 60 °C (Supplementary Materials, SP. 2A). Doubling the equilibration time for each measurement point did not change the isotherm nor the hysteresis shape (SP. 2B, cf. SP. 1). Rehydration and repeated measurement of Li-Mtm after predrying at 210 °C, however, resulted in a perfect overlap of the isotherms (SP. 2C), implying that the minor imperfection in repeatability of the isotherm and the hysteresis observed come only from minor variability in the in-situ dehydration conditions (cf. Fig. 1B, E).

### 4.2. Low-pressure gas adsorption

According to IUPAC classification (Thommes et al., 2015), all the measured nitrogen adsorption isotherms on smectitic samples (Fig. 3A–G) were type IV(a), having a H3 or H4 hysteresis loop, characteristic for mesoporous platy-like shaped materials. Different $N_2$ isotherm types were observed for illites (Fig. 3H). LePUY(f) showed a typical IV(a) isotherm type, and H2(b) hysteresis loop type, commonly resulting from materials with mesopore necks, blocking the mesopores, whereas the adsorption isotherm on Zempleni (IUPAC isotherm type III, without hysteresis) corresponds to a non-porous material. Almost all isotherms (except Zempleni) presented a high component of the I type IUPAC isotherm, associated with microporosity (Thommes et al., 2015). The isotherm obtained on Orient_Na_Mtm(f) (Fig. 3F) showed significantly higher hysteresis than that on Disorient_Na_Mtm(f).

The $N_2$ micropore volumes calculated with t-plot and DR methods returned very similar values, and generally follow the 1:1 trend line, as presented in Fig. 4B, with one outliner (LePUY(f)). As the DR method was used also for the calculation of micropore volumes from $CO_2$ adsorption isotherms, the results from DR method ($V_{m\_DR\_N2}$) will be used hereafter in the paper.

Texture parameters calculated from $N_2$ adsorption isotherms are shown in Table 1. Generally, an increase of the drying temperature, increased a smectite's $N_2$-available microporosity, which is not the case for Mg-exchanged smectites, for which drying at 110 °C decreased $V_{m\_DR\_N2}$ even by 80% (Table 1; Fig. 5). TMA_Mtm sample showed much higher $V_{m\_DR\_N2}$ than the other Mtm samples, and the value almost doubled with the drying temperature, from 60 and 315 °C: from 0.065 cc/g to 0.110 cc/g, respectively (Fig. 5). Orient_Na_Mtm(f) showed a little higher $V_{m\_DR\_N2}$ than Disorient_Na_Mtm(f). For LePUY(f) illite $V_{m\_DR\_N2}$ was five times greater than for Zempleni, 0.043 cc/g and 0.008 cc/g, respectively. However, according to the t-plot model, both illites show a much lower micropore volume than from the DR method, 0.008 cc/g for LePUY(f) and < 0.001 cc/g for Zempleni.

SSA calculated using the BET algorithm reached from 22.1 $m^2$/g for Mg_BId(f)_210Cpt sample to 273.1 $m^2$/g for the TMA_Mtm_315Cpt sample and linearly followed $V_{m\_DR\_N2}$ (Fig. 4C), except for LePuy(f) and Li_Mtm_210Cpt samples. The linear relationship with $V_{m\_DR\_N2}$ was expected for the samples in which adsorption sites in micropores dominate over those located elsewhere as the BET model developed for non-microporous materials includes a component that is dependent on the microporous contribution (Rouquerol et al., 2007). Drying at higher temperatures generally increased SSA BET, except for Mg-exchanged smectites, where a significant decrease after drying at 110 °C was observed.

The external surface area (ESA) was not sensitive to drying conditions and did not vary significantly between different cation forms and different samples, reaching from 20.1 to 46.1 $m^2$/g, except Na_Mtm(f) with lower ESA values (12.8 and 18.9 $m^2$/g for Disorient and Orient_Na_Mtm(f), respectively) and much higher ESA for LePUY(f) (153.1 $m^2$/g).

$CO_2$ adsorption on clay mineral samples resulted in two distinct groups of isotherms, with different shape and maximum (Fig. 6). The first group (TMA- and Cs-exchanged smectites, and Mg-exchanged smectites dried at 60 °C) showed a steep increase in the low $p/p^0$ region and high adsorption at the maximum pressure. Microporosity calculated from the $CO_2$ adsorption isotherms ($V_{m\_DR\_CO2}$) for these samples was in the range of 0.070 cc/g to 0.106 cc/g (Table 1). All the other samples, except Ca_Mtm_60Cpt, belong to the other group of $CO_2$ adsorption isotherms, characterized by the less steep isotherm at low pressure and significantly lower maximum $CO_2$ adsorption, resulting in significantly lower $V_{m\_DR\_CO2}$ than the first group of samples. Two illites showed spectacularly different micropore volume: 0.010 cc/g for Zempleni_210Cpt to 0.039 cc/g for LePuy(f)_210Cpt. The $CO_2$ adsorption isotherm for Ca_Mtm_60Cpt was intermediate between the first and second isotherm groups ($V_{m\_DR\_CO2}$ = 0.056 cc/g). All $CO_2$ adsorption

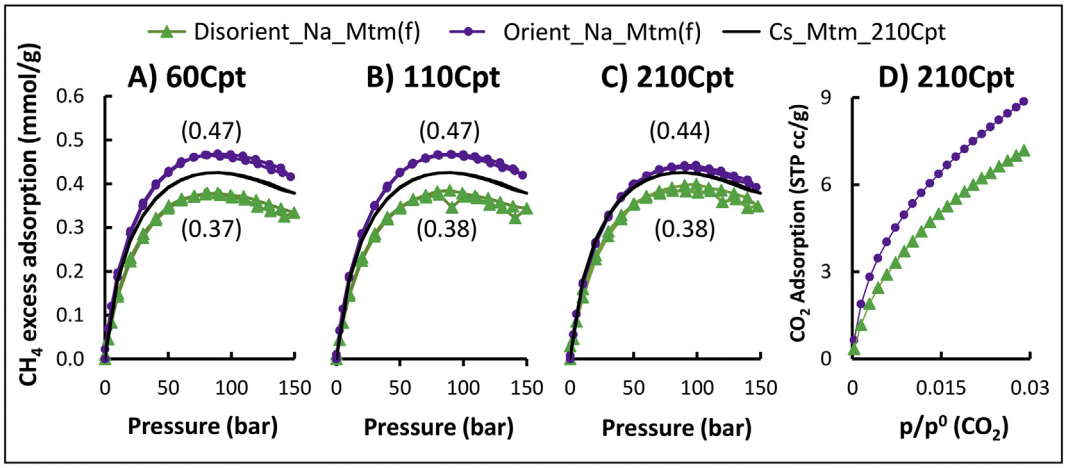


**Fig. 2.** $CH_4$ and $CO_2$ adsorption isotherms on highly oriented (violet) and freeze-dried (green) Na-exchanged montmorillonite (fraction < 2 μm), after drying at specified temperature. Cs-exchanged isotherm added as a reference. Maximum excess $CH_4$ adsorption added in brackets (mmol/g).

isotherms are presented separately in Supplementary Materials (SP. 3).

### 4.3. Transmission electron microscopy

TEM photographs of Mtm(f), BId(f), LePUY(f), and Zempleni samples are shown in Fig. 7 A–D. Mtm(f) and BId(f) samples were well dispersed and their fundamental particles remained mostly isolated on the TEM holder. Their crystallites had irregular but well-defined edges. Zempleni illite particles were mostly columnar, with a high tendency to aggregate. LePUY(f) illite showed very fine, barrel shape crystallites, very similar to that observed by Rajec et al., (1999). Large aggregates of the LePUY(f) crystallites were also observed.

Planar surface areas of fundamental particles were calculated using ImageJ software (Schneider et al., 2012). Twenty (Zempleni) to 200 (LePUY(f)) measured surfaces were used for dimensions' statistics. The finest and largest particles were observed for the illitic samples, with the average diameters of 33 ± 8 nm for LePUY(f) (~1000 $nm^2$/particle) and 396 ± 108 nm for Zempleni (~123,000 $nm^2$/particle). The average diameters of the smectites were from 146 ± 56 nm for Mtm(f) (~17,000 $nm^2$/particle) to 321 ± 109 nm for BId(f) (~81,000 $nm^2$/particle).

### 4.4. Thermogravimetric analysis

Thermogravimetric (TG) analysis allowed estimations of the content of clay-bound water remaining after each drying step, based on the clay mineral chemical formula. The mass of sample at 1000 °C was considered to be completely dehydroxylated and used as a reference mass (cf. Kuligiewicz and Derkowski, 2017), with an assumption that dehydroxylation does not occur at or below 210 °C.

The clay-bound water content was calculated based on the measured mass loss and normalized on the interlayer cation content. For the smectite samples exchanged with an inorganic cation, the observed mass loss directly comes from the loss of adsorbed water. However, in the case of TMA-exchanged Mtm the mass loss comes not from dehydration, but from the decomposition of the $TMA^+$, thus resulting in greater mass loss at 210 °C than at 110 °C (opposite to dehydration). $TMA^+$ decomposition was confirmed to occur above 200 °C using mass spectroscopy of the evolved gas during ramp-heating TG experiments (data not shown). Therefore, the apparent adsorbed water content calculation for TMA_Mtm was not presented in Fig. 5.

The content of adsorbed water per one exchengable cation for Mtm decreases with the increase of drying temperature, and generally decreases with the interlayer cations' hydration enthalpy (Fig. 5; cf. Kuligiewicz and Derkowski, 2017). The smectites exchanged with monovalent, inorganic cations ($Cs^+$, $Li^+$) had significantly lower adsorbed water content (from 0.8 after drying at 60 °C down to 0.1 after drying at 210 °C) than Mg-, Ca-exchanged samples (from 4.0 to 0.7 $H_2O$ moleclues per cation). Drying curves are shown in detail in the supplementary materials (SP. 4). Adsorbed water content remaining after an isothermal drying step was similar in the methane adsorption chamber and in the TG experiments, however in the case of drying at 60 °C, drying in the TG instrument seemed to be more efficient (see supplementary information SP. 5).

### 4.5. X-ray diffraction

X-ray diffraction patterns were collected on an oriented powder and are therefore, supposed to represent only the *00l* reflection series (Fig. 8). TMA_Mtm and Cs_Mtm showed a constant basal spacing of 1.37 and 1.13 nm, respectively, insensitive to drying temperature. All other samples showed a continuing decrease of the basal spacing upon drying: Mg_Mtm shifted its basal spacing from 1.18 nm (60 °C) to 1.08 nm (at 210 °C). Drying at 110 °C strongly decreased Li- and Ca_Mtm basal spacing from 1.08 to 1.01 nm and from 1.12 to 1.02 nm respectively. After drying at 210 °C both these samples showed ~1.00 nm basal spacing, corresponding to a contracted interlayer.

## 5. Discussion

### 5.1. Clay mineral interlayer state

The removal of tightly bound water in clay minerals is mostly controlled by drying temperature (Ferrage et al., 2007b; Kuligiewicz and Derkowski, 2017). In a case of expandable clay minerals, where the adsorbed water content can change significantly, the same sample dried at different conditions can return different results due to different behavior of interlayer cations, layer stacking, and the width of interlayer space.

Drying at 60 °C decreased the amount of water moleclues in all samples to much less than the number corresponding to the first hydration shell. That is the case even for $Mg^{2+}$ having the highest hydration enthaply among all cations used (4 $H_2O$/cation after drying at 60 °C vs 6 $H_2O$/cation for full first hydration shell; Fig. 5, cf. SP. 4). In such a water-deficient state, water moleclues are coordinated directly to the interlayer cations (Cases et al., 1997; Ferrage et al., 2007a; Kuligiewicz and Derkowski, 2017), acting like pillars for the interlayer and leaving vacancies outside of the first hydration shell volume. There is a specific number of $H_2O$ molecules adsorbed in single plane around the interlayer cations which prevents the interlayer gallery contraction

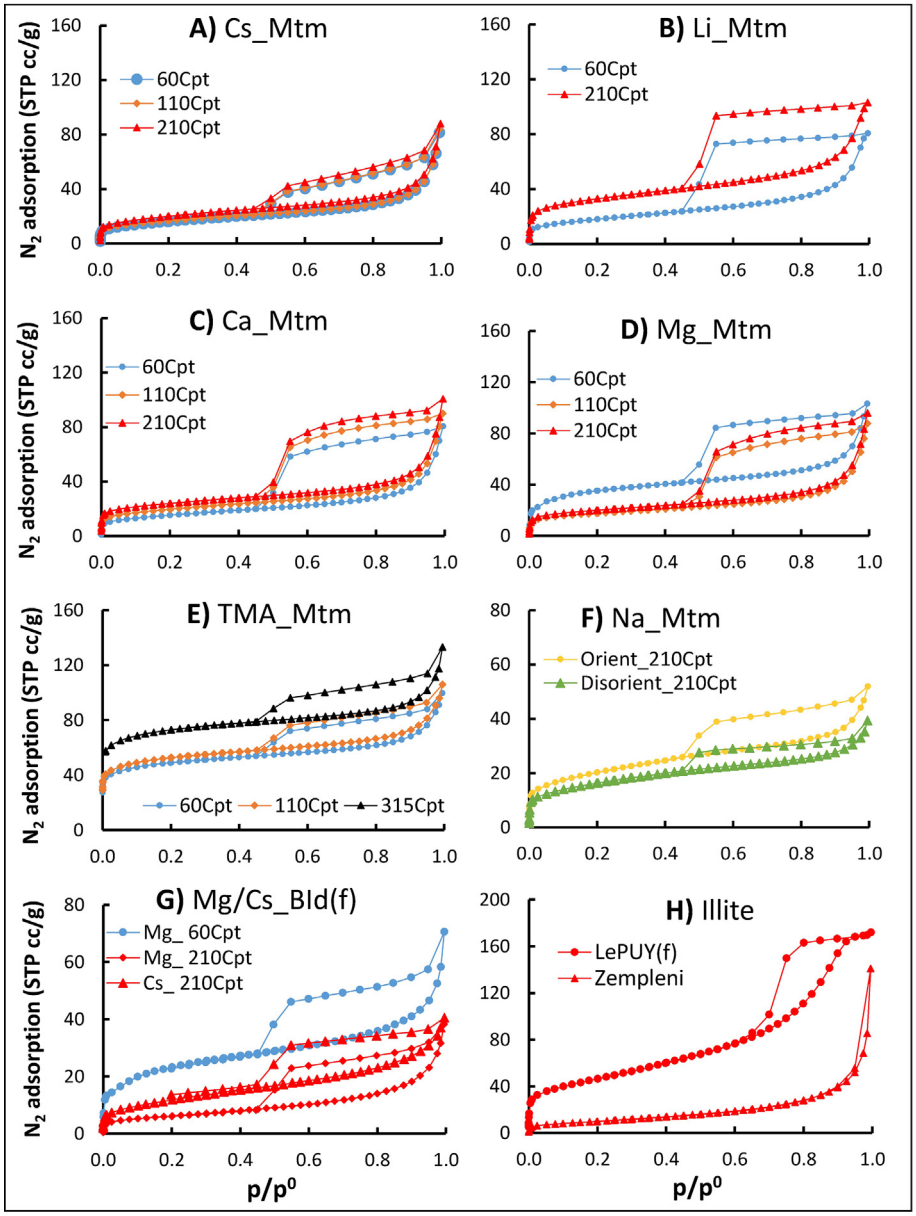


**Fig. 3.** Nitrogen adsorption isotherms obtained at −196 °C on cation-exchanged montmorillonite (SAz-1), beidellite (SBId-1), illites (LePUY and Zempleni): after drying at specified temperature.

and binding the cations to oxygen in ditrigonal cavities, resulting in decreased basal spacing. Hovewer, dehydrated $Cs^+$ and $TMA^+$ are the exceptions as their large dimensions prevent the interlayer contraction to the same extent as for smaller cations, even without the presence of the water hydration shell.

Based on the adsorbed water content of ~4.0 and ~2.3 $H_2O$/cation (Fig. 5), relatively large avarage basal spacing (≥1.17 nm), and the relatively narrow XRD *001* reflection that suggest narrow distribution of interlayer widths (Fig. 8), Mg-exchanged Mtm dried at 60 °C and 110 °C must have mostly uncontracted interlayers. Similar water contents measured for the Mg_BId(f) sample suggest that the sample was analogous to Mg_Mtm in terms of the interlayer thickness after drying at the corresponding temperature (cf. SP. 4). Ca_Mtm_60Cpt showed similar water content to Mg_Mtm_110Cpt, however, the average basal spacing was lower than that for the Mg-exchanged sample. For such a Ca-exchanged montmorillonite hydration state (~2 $H_2O/Ca^{2+}$) Ferrage et al. (2007a) found that about 40% of layers were still not contracted and ca. 1.18 nm thick. Drying of Mg-exchanged smectites at 210 °C and Ca-exchanged montmorillonite at 110 °C led to dehydration and the clousure of interlayer galleries (see Fig. 5).

All the other inorganic cations present in the interlayer galleries allowed strong dehydration, and interlayer contraction even at 60 °C. The interlayer contraction corresponds to low average adsorbed water content, less than 0.8 $H_2O$ molecule/cation, whereas at least ~1.25 $H_2O$ molecule/cation is needed to support 20% of non-contracted interlayers in Na-exchanged montmorillonite (Ferrage et al., 2010). Due to the large size of $Cs^+$, the interlayer of Cs_Mtm and Cs_BId(f) did not contract to the same width as smectites saturated with smaller cations (cf. Ferrage et al., 2007b), irrespective of drying temperature and water content (Fig. 5, cf. SP. 4).

Due to the extremely hydrophobic nature of $TMA^+$ compared to inorganic cations, it is not surrounded by $H_2O$ in the TMA_Mtm' interlayer. The calculated water mass loss must be related to thermal decomposition of excess TMA adsorbed at the outer surfaces of smectite crystallites; therefore, it did not affect the d-space upon heating. Due to the large size of the $TMA^+$, the interlayer remained fully open even

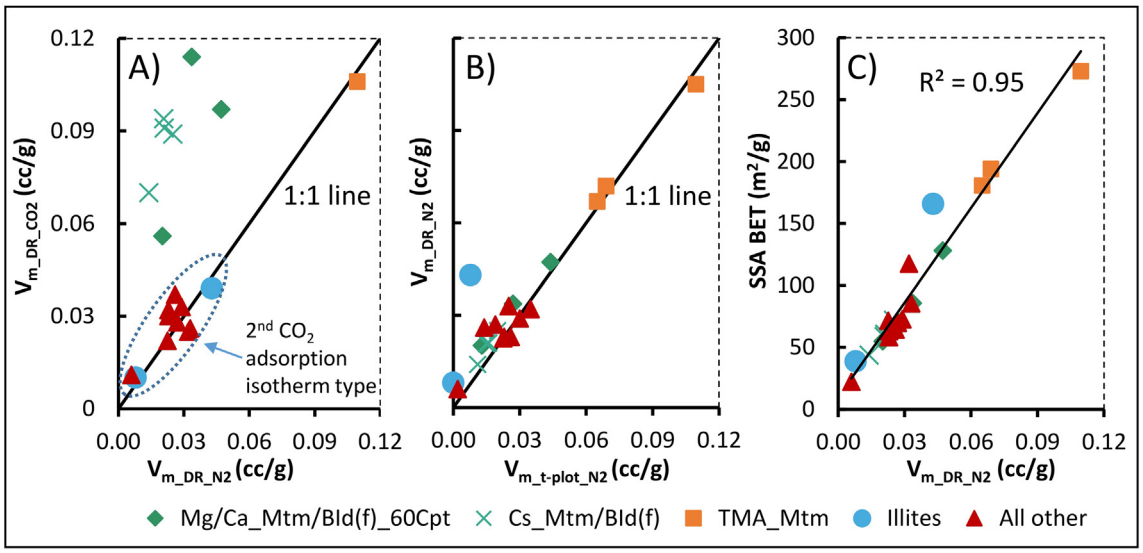


**Fig. 4.** Comparison of clay minerals texture parameters ($CO_2$ and $N_2$ micropore volume calculated using DR and t-plot method, and specific surface area BET). Clay mineral samples were split into classes. Blue-dotted area include samples that showed 2nd $CO_2$ adsorption type. (For interpretation of the references to colour in this figure legend, the reader is referred to the web version of this article.)

after drying at 315 °C (Fig. 5).

### 5.2. Structural and textural interplay

Each drying step at a subsequently higher temperature, resulted in the removal of a subsequent fraction of adsorbed water, which decreases the sample's reference mass. The progressing dehydration is expected to virtually increase the content of adsorbed gas by a factor equivalent to the mass of water lost during the drying step (Fig. 3, cf. SP. 4). However, the observed increase in $N_2$ adsorption, thus, in microporosity and SSA BET, cannot be explained by that mechanism, as the relative decrease of the sample weight was insignificant (maximum 3.7% relative) with respect to the change in $V_{m\_DR\_N2}$ or SSA BET. After taking into account different residual water content and normalizing the texture parameters on the dry mass, the trends with drying temperature were retained, as presented in Fig. 5. Therefore, the observed increase in microporosity with drying temperature is assumed to originate from the subsequent removal of water molecules or $TMA^+$ that were occupying the micropores.

It is generally believed that $N_2$ does not penetrate smectite interlayers, mainly due to limited diffusivity in such narrow micropores at the cryogenic conditions of the measurement. The majority of $N_2$ is adsorbed on the basal planes of smectite crystallites, and in the meso- and micropores formed due to irregular stacking of the clay mineral layers, with microporosity located mainly at the edges of the crystallites (Kaufhold et al., 2010; Michot and Villiéras, 2006). Such an adsorption model indeed corresponds to relatively low $V_{m\_DR\_N2}$ found for all Mtm samples exchanged with an inorganic cation, due to the interlayer inaccessibility for $N_2$, regardless of the drying temperature (Fig. 5; Table 1). In contrast, due to a large basal spacing (~1.37 nm), $N_2$ easily intercalates TMA-smectite, what was also observed by Barrer and MacLeod (1955) and Rutherford et al., (1997); partial removal of excess TMA during drying at 315 °C without decreasing the interlayer width further increases interlayer availability for $N_2$. Significant decrease of $V_{m\_DR\_N2}$ after drying at 110 °C (Fig. 5) combined with d-space of 1.18 nm, however, suggests at least partial interlayer accessibility for $N_2$ in Mg-exchanged smectite dried at 60 °C. For any other interlayer opening, corresponding to *001* d-space of 1.17 nm and lower, $N_2$ seems not to penetrate the interlayer, therefore, the calculated $V_{m\_DR\_N2}$ should be independent of the clay mineral structure. Indeed, the agreement between $V_{m\_DR\_N2}$ and the crystallites planar dimension regardless of the sample interlayer state (Fig. 9) suggests a textural control on $N_2$-based microporosity. These results are in contrast to Chiou and Rutherford (1997) who suggested partial $N_2$ diffusion in a Cs-exchanged SAz-1 sample after finding ~40% higher micropore volume and higher SSA BET for the Cs-exchanged form in respect to the $Ca^{2+}$ and $Na^+$ forms of SAz-1 Mtm.

SSA BET corresponds to strong retention capacity; for microporous materials it thus strongly depends on the micropore volume (Rouquerol et al., 2007). In the case of the clay minerals studied, microporosity is the main controlling factor of SSA BET, therefore SSA BET values linearly follow $V_{m\_DR\_N2}$ (Fig. 4c) and any changes in $V_{m\_DR\_N2}$ or $V_{m\_t\text{-}plot\_N2}$ of smectite samples are reflected in their SSA BET (see Fig. 5; cf. $V_{m\_DR\_N2}$ and $V_{m\_t\text{-}plot\_N2}$ in Fig. 4B). Therefore, the calculated ESA represents only a small fraction of SSA BET (Table 1). Due to contracted interlayers during $N_2$ adsorption, SSA BET calculation does not reflect the total specific surface area (TSSA) of the smectites' fundamental particles, (700–750 $m^2/g$) which is measured with polar liquids (Środoń et al., 2009). ESA remains very low in respect to TSSA, as it measures only the external surfaces of crystallites. If calculating based on TSSA, ESA corresponds to tactoids formed by 20–25 layers whereas 30–40 layers form BId. Insensitivity of $N_2$ adsorption isotherms' at $p/p^0 > 0.2$ (Fig. 3) to drying temperature resulted in the lack of significant changes in calculated ESA after each drying step (Table 1).

In contrast to $N_2$ adsorption under cryogenic conditions, $CO_2$ easily enters ultramicropores even narrower than 0.7 nm (Cazorla-Amorós et al., 1998; Lowell et al., 2004). All the samples that showed the second type of $CO_2$ adsorption isotherm resulted also in very similar $V_{m\_DR\_N2}$ and $V_{m\_DR\_CO2}$ values (Fig. 4A), following the 1:1 trend line. The high correlation of micropore volumes measured by the $N_2$ and $CO_2$ and the fact that $N_2$ has very low interlayer penetrability due to its small diffusivity in micropores narrower than 0.7 nm (interlayer ca. 0.33 nm for Li_Mtm_60Cpt and 0.25 nm for Ca_Mtm_210Cpt) indicates that both, $CO_2$ and $N_2$ were adsorbed in the equivalent adsorption sites, in microporosity located outside of the interlayer galleries. These conclusions are in agreement with the results of Loganathan et al., (2018), who showed that $CO_2$ does not enter the dehydrated interlayers of Li-, Na-, Mg-, and Ca-exchanged smectites. High agreement between $V_{m\_DR\_N2}$ and $V_{m\_DR\_CO2}$ was also observed for the TMA-exchanged Mtm sample. However, in contrast to the samples with a fully contracted interlayer, the matching micropore volume comes from a complete filling of the TMA-smectite interlayer by both probe gases.

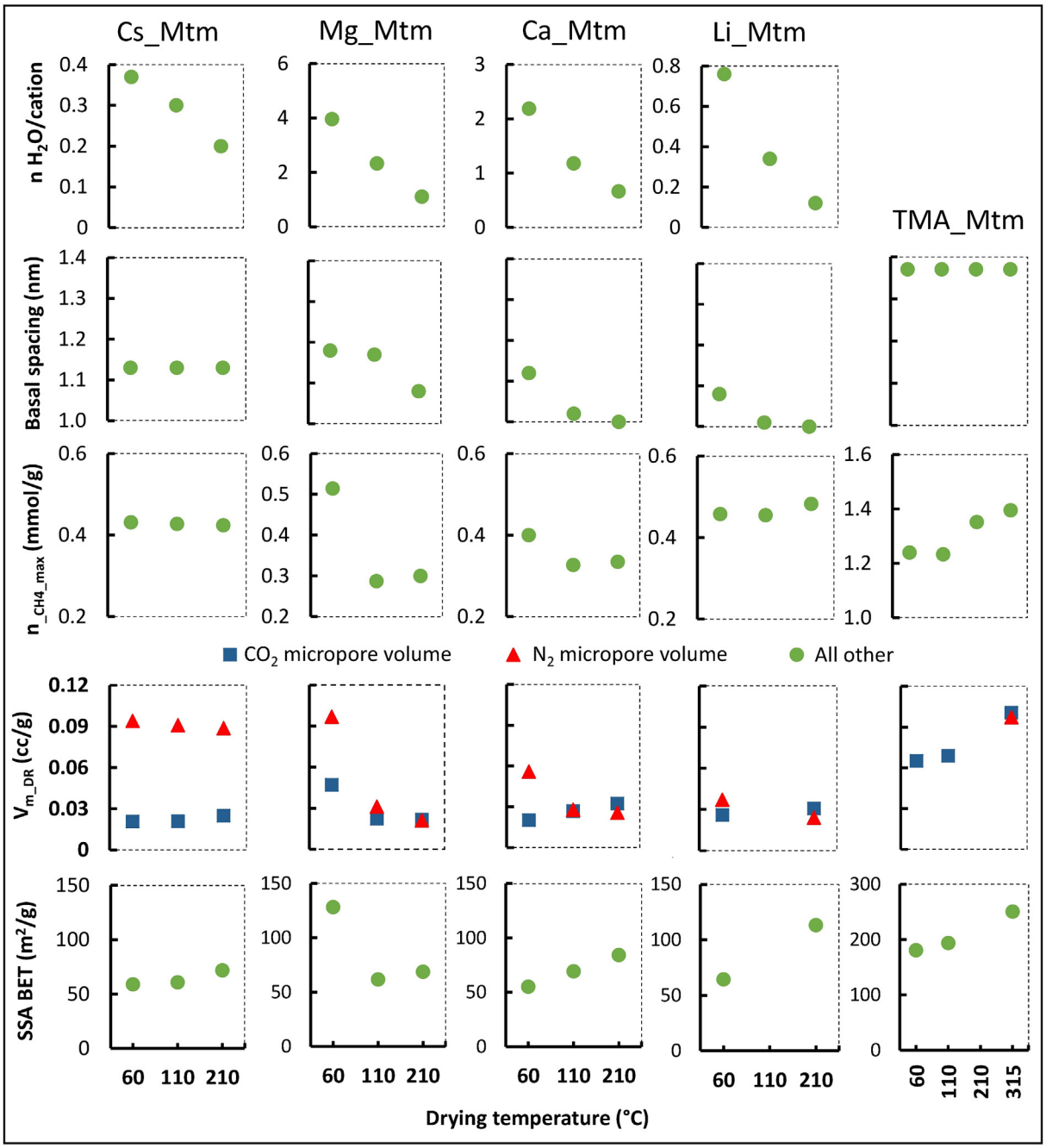


**Fig. 5.** Number of water molecules per exchangeable cation, basal spacing, maximum high-pressure excess adsorption of methane, $N_2$ and $CO_2$ microporosity and specific surface area BET for Cs-, Mg-, Ca-, Li-, and TMA- exchanged SAz-1 montmorillonite, after drying at specified temperatures. All results (except number of water molecules per cation and basal spacing) were normalized for mass loss during drying.

All the Cs-exchanged smectites and Mg- and Ca-exchanged smectites dried at 60 °C, present $CO_2$-based micropore volume higher than their $N_2$-based counterparts (Fig. 4A) indicating at least partial adsorption of $CO_2$ in the interlayers. Indeed, Loganathan et al., (2018) predicted no energy barrier for $CO_2$ intercalation into completely dry Cs-exchanged hectorite, and the possibility of $CO_2$ intercalation in the Mg-exchanged hectorite that begins at 1.07 nm basal spacing and reaches the first plateau for ~1.20 nm basal spacing. Additionally, $CO_2$ has been proven experimentally to intercalate expandable clay minerals under low pressure (Aylmore, 1974; Fripiat et al., 1974) and high pressure (Bowers et al., 2017; Giesting et al., 2012a, 2012b; Romanov, 2013). When entering the interlayer, dry $CO_2$-induced swelling was observed for expandable clay minerals (Bowers et al., 2017; Giesting et al., 2012a, 2012b; Loganathan et al., 2018). After drying at 110 °C or higher temperature, the interlayer of Mg-exchanged and Ca-exchanged smectites closes enough to prevent the intercalation of both $CO_2$ and $N_2$, resulting in a close to 1:1 relationship of micropore volume calculated from these isotherms (Fig. 4A). Interestingly, this reduction of $N_2$ and $CO_2$ accessibility in the interlayer is related to only a subtle decrease of the interlayer width by only ca. 0.01 nm of Mg_Mtm (basal spacing from 1.18 to 1.17 nm; Figs. 5 and 8).

Combining $V_{m\_DR\_CO2}$ and the mineral density calculated based on the XRD data, chemical formula, and adsorbed water content, $CO_2$-available microporosity stands for 26% of total volume of Cs_Mtm_210Cpt, 22% of TMA_Mtm_315Cpt, 24% of Mg_Mtm_60Cpt, versus only 7% of Mg_Mtm_110Cpt, and 7% and 6% of completely

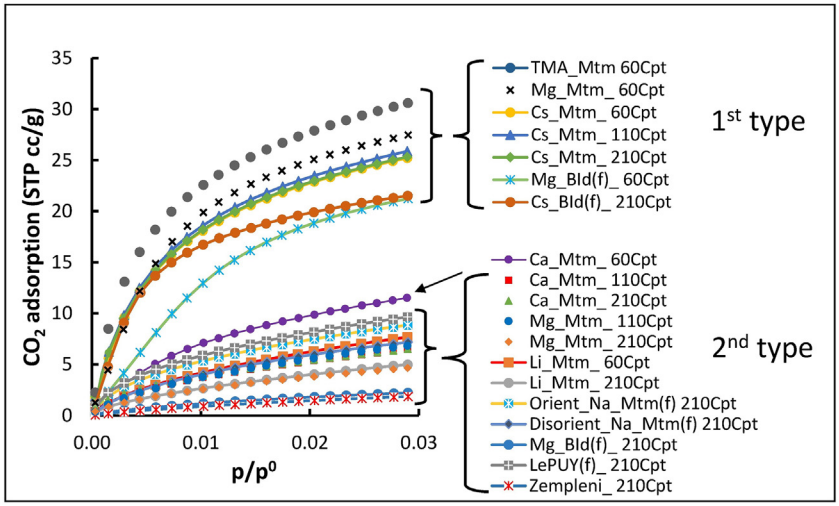


**Fig. 6.** Carbon dioxide adsorption isotherms obtained on cation-exchanged montmorillonite (SAz-1), beidellite (SBId-1), illites (LePUY and Zempleni) at 0 °C after drying at a specified temperature.

contracted Ca_Mtm_210Cpt, and Li_Mtm_210Cpt, respectively. If the latter samples are assumed as a baseline structure for zero-interlayer availability thus corresponding to micropores developed between the crystallites, 15 to 20% of the former smectite crystal structure is available for $CO_2$ diffusion, which corresponds to roughly half of the total interlayer volume.

ESA is sample-specific, directly related to the clay crystallite planar dimension (Fig. 9). Geometry of individual clay particles impacts also micropore volume (Fig. 9B, C), Generally, the finer the clay crystallites, the greater the crystallite edges, thus higher external free surface (ESA) and the higher $V_{m\_DR\_N2}$, due to lesser probability of ideal parallel face-to-face stacking that prevents the formation of microporosity. Textural parameters of fully randomized and oriented smectite particles present, however, another extreme case: greater distance between crystallites (or tactoids) and more face-to-edge stacking decreases the ability to adsorb $CO_2$ and $N_2$ between crystallites (Figs. 2D, 3F, Table 1). The generally lower ESA of the separated fractions than bulk Mtm samples also results from better stacking of smectite fundamental particles when not disturbed by non-clay impurities. It is thus not only the crystallite dimensions, but also the way they are assembled in a rock or a sediment that controls the gas adsorption properties.

Maximum $CO_2$ pressure reached at the temperature applied during measurements corresponds to complete filling of micropores narrower than 1.5 nm and incomplete filling of larger micropores (Cazorla-Amorós et al., 1998). Perfect 1:1 agreement obtained for $N_2$- and $CO_2$-based micropore volumes for the samples with $CO_2$-unavailable interlayer (Fig. 4A) and 1:1 agreement of $V_{m\_DR\_N2}$ and $V_{m\_t\text{-}plot\_N2}$ (Fig. 4B) allow the conclusion that the applied $CO_2$ adsorption conditions results in the equivalent of $CO_2$ filling the < 2 nm micropore volume.

### 5.3. Methane-accessible surface in clay minerals

Almost exactly the same linear correlations were observed between $n_{\_CH4\_max}$ and $V_{m\_DR\_N2}$ and between $n_{\_CH4\_max}$ and SSA BET ($R^2$ = 0.88 and 0.89, respectively; Fig. 10A, B), as it is mainly the microporosity that controls SSA BET in the analyzed samples (see discussion in 5.2. subsection; Fig. 4C). Although not having a meaningful interpretation for microporous adsorbents' surface area, SSA BET is widely used in the literature and therefore handy for data comparison. Because ESA showed no correlation with $n_{\_CH4\_max}$ (Fig. 10D), microporosity accessible for $N_2$ must be the major control on the $CH_4$ adsorption in clay minerals. Indeed, all the samples that had matching $V_{m\_DR\_N2}$ and $V_{m\_DR\_CO2}$, thus similar interlayer accessibility for $N_2$ and $CO_2$ show a significant linear correlation between $n_{\_CH4\_max}$ and $V_{m\_DR\_CO2}$ (Fig. 10C), whereas the samples with higher interlayer accessibility for $CO_2$ greatly depart from that trend line. Despite the measurement conditions (temperature thus diffusivity) of $CH_4$ adsorption similar to those for $CO_2$ adsorption rather than cryogenic $N_2$ adsorption, $CH_4$ fills the adsorption sites corresponding to $N_2$. If $CO_2$ adsorption in the smectite interlayer is indeed driven by the combination of accessibility (~0.30 nm $CO_2$ axial dinension vs ~0.38 nm for the tethaedreal $CH_4$; Liu et al., 2015) and swelling, $CH_4$ does not follow $CO_2$ behavior. If $CH_4$-induced swelling occurs in smectites, it must be much less pronounced than for $CO_2$.

Even partially open interlayers of Mg- and Ca-exchanged smectites are available for $CH_4$. The H-type adsorption isotherm presented by the smectites exchanged with divalent cations and dried at 60 °C consists of mixed adsorption, occurring both on external features of crystallites and in the interlayers. However, the interlayer adsorption is far lower than that occurring in fully available TMA_Mtm. Although the hysteresis may indicate the lack of complete equilibration (cf. SP. 1) it corresponds to relative equilibrium between the adsorption and desorption paths, which comes from the energetic barrier either delaying the diffusion into narrow interlayer galleries (e.g. slow interlayer swelling) or delaying the diffusion out of the interlayer due to repositioning of cations and $H_2O$ in a $CH_4$-filled interlayer (cf. Whitley and Smith, 2004). Similar hysteresis was observed for high-pressure $CO_2$ adsorption on montmorillonite (Jeon et al., 2014), which is known to swell under $CO_2$ pressure if interlayer galleries are wide enough (Bowers et al., 2017). Basal spacing of Mg_Mtm_110Cpt of ca. 1.17 nm, very close to the 1.15 nm intercalation threshold proposed by Bowers et al., (2018), might explain residual hysteresis between $CH_4$ adsorption and desorption isotherms observed for Mg-exchanged smectites, dried at 110 °C (Fig. 1 B, G). Even though having a lower average basal spacing than the 1.15 nm $CH_4$ intercalation threshold (Bowers et al., 2018), Ca-exchanged Mtm dried at 60 °C still had a portion of non-contracted interlayers (see 5.1. discussion), therefore, the decrease in $n_{\_CH4\_max}$ after drying at 110 °C was much lower than for Mg_Mtm (cf. Fig. 1B, D).

### 5.4. Applications to high-pressure methane adsorption in rocks and sediments

Besides the interlayer accessibility, it is the clay particles planar dimensions that mainly control methane adsorption capacity, following the same control on micropore volume and ESA measured by $N_2$ adsorption (Fig. 9). To a lesser degree, $n_{\_CH4\_max}$ is affected by the clay particles' pattern of aggregation and mutual relationships in a sediment (Fig. 2D). Those structure-independent factors highly influence gas

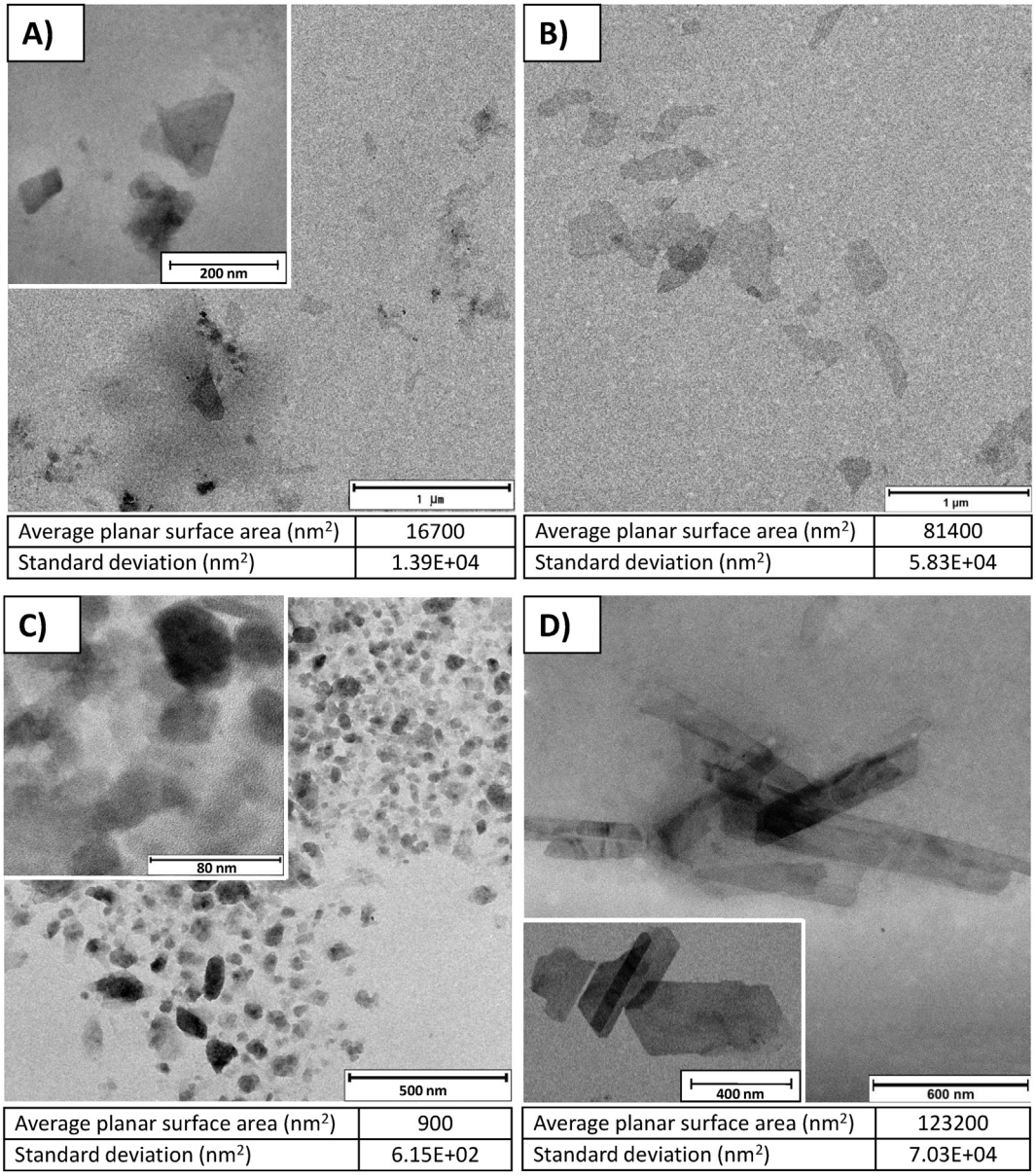


| Average planar surface area (nm²) | 16700 |
|---|---|
| Standard deviation (nm²) | 1.39E+04 |

| Average planar surface area (nm²) | 81400 |
|---|---|
| Standard deviation (nm²) | 5.83E+04 |

| Average planar surface area (nm²) | 900 |
|---|---|
| Standard deviation (nm²) | 6.15E+02 |

| Average planar surface area (nm²) | 123200 |
|---|---|
| Standard deviation (nm²) | 7.03E+04 |

**Fig. 7.** TEM photographs of A) SAz-1 montmorillonite, B) SBId-1 beidellite, C) Le PUY illite, D) Zempleni Illite. Average planar surface area below the photographs.

(including methane) adsorption behavior and they are likely the reason for strong inconsistences found in the literature for adsorption on, apparently, the same clay mineral species (Cheng and Huang, 2004; Heller and Zoback, 2014; Ji et al., 2012; Liu et al., 2013; Ross and Bustin, 2009).

Our study presents methane adsorption on illite and on smectite with the interlayer contracted by complete drying, fully open by pillaring (TMA-Mtm), or partially dried and pillared by cations having a residual water shell. Such a dry-end state of clay minerals corresponds to the conditions commonly used for high-pressure methane adsorption in natural mudrocks (Gasparik et al., 2014; Rexer et al., 2013, 2014; Topór et al., 2017a, 2017b). At a higher hydration state, the smectite interlayer opens to an extent that allows methane diffusion. However, water needed to support the interlayer opening ultimately fills the interlayer and larger external pores to the extent of blocking the methane molecules (Bowers et al., 2018; Li et al., 2016; Rao et al., 2013; Rao and Leng, 2014). In so-called gas shales which are the self-sourcing $CH_4$ reservioirs, thus thermally mature black shales, illite and interstratified illite-smectite mineral with a low fraction of expandable interlayers (< 20%) are the dominating clay minerals (e.g. Wilson et al., 2016). Therefore, besides organic matter (Topór et al., 2017b) the geometry of illite fundamental particles and the way they assemble are the controlling factors of the total $CH_4$ adsorption capacity in gas shales. Under favourable hydration state, however, minor fractions of expandable layers might provide additional adsorpion sites even in a strongly illitised rock.

Good linear correlations of clay minerals' $N_2$–based micropore volume and SSA BET with maximum methane adsorption is in contrast to the relationships observed for natural clay-rich and organics-rich shale samples (Fig. 10). In mudrocks, instead of the $n_{CH4\_max}$ correlation with $V_{m\_DR\_N2}$ and SSA BET, a linear trend follows $CO_2$-based microporosity due to the overwhelming microporosity in organic matter, which is inaccessible for $N_2$ under cryogenic conditions. The linear correlation between $V_{m\_CO2}$ with $n_{CH4\_max}$ that is commonly observed for natural samples and separated solid organic matter (kerogen) (Rexer et al., 2014; Topór et al., 2017b) occurs only in the clay mineral samples that do not swell in the $CO_2$ atmosphere. That trend is not followed for the clay mineral samples with presumed $CO_2$-induced swelling.

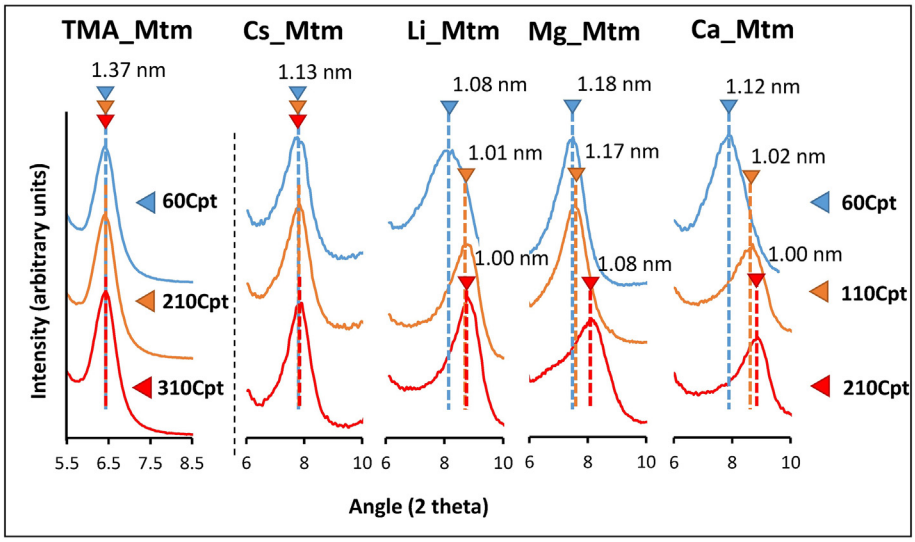


**Fig. 8.** XRD *001* reflections obtained after 10 h of drying at 60, 110 and 210 °C of various cation-forms of SAz-1 montmorillonite (60, 210, and 310 °C for TMA_Mtm).

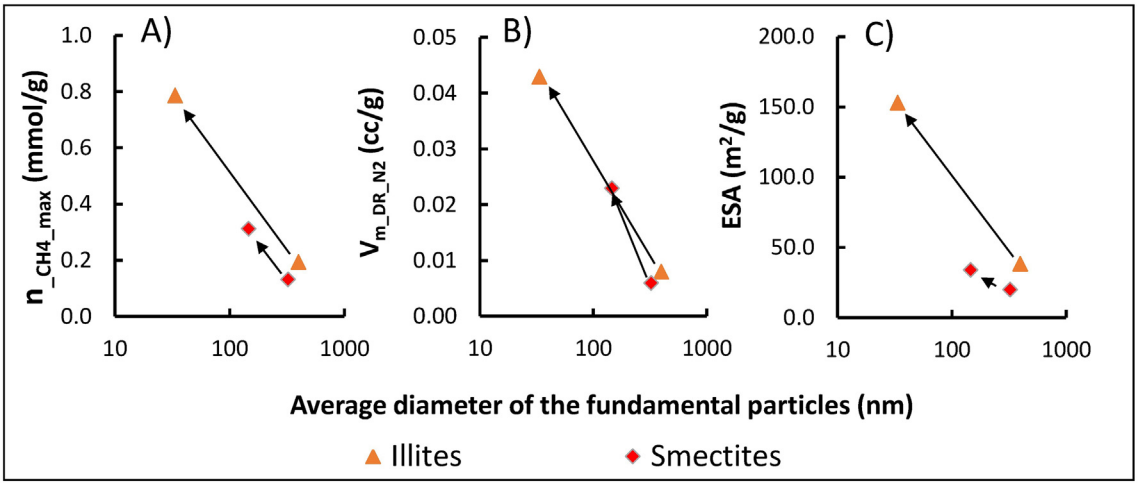


**Fig. 9.** High-pressure methane maximum excess adsorption, $N_2$ micropore volume and external surface area as a function of average diameter of the fundamental particles of the clay minerals particles measured by TEM (in logarithmic scale).

## 6. Conclusions

Methane adsorption sites in clay minerals dried under vacuum correspond to those accessible to nitrogen molecules adsorbed under cryogenic conditions. Adsorption capacity is primarily controlled by the clay particles texture. The adsorption sites are located mainly in the micropores generated between imperfectly stack layers and crystallites, and on the external surface of the crystallites. Large organic cations such as tetramethylammonium, located in the interlayer of expandable clay minerals act as pillars, allowing intercalation of $CH_4$ in the interlayer galleries. However, a significant amount of $CH_4$ can enter the interlayer of smectites exchanged with divalent cations of high hydration enthalpy. Residual water remaining after extensive drying, even at elevated temperatures, forms a strong complex with the interlayer cation, which prevents interlayer contraction. Higher water loading results in a wider interlayer opening, however, $H_2O$ blocks the sites potentially available for $CH_4$, decreasing methane adsorption capacity. The adsorbent texture is strongly controlled by the crystallites planar dimensions and is not related to the particular clay mineral type. The textural control on $CH_4$ adsorption that is independent of the mineral structure probably accounts for reported inconsistences in maximum $CH_4$ adsorption for the same clay mineral species. In contrast to pure clay minerals, $CH_4$ adsorption capacity in natural, organic-rich mudrocks and shales, shows a good correlation with $CO_2$-measured microporosity rather than microporosity calculated from $N_2$ adsorption. Fast and inexpensive $CO_2$ adsorption measurements are assumed to provide a good proxy for the estimation of methane adsorption capacity in rocks and sediments. However, higher penetrability of $CO_2$ than $CH_4$ in the interlayer opening corresponding to the d-space between 1.12 nm (incompletely contracted interlayer) to 1.18 nm (the largest d-space tested for inorganic cations), results in the overestimation of a sample's $CH_4$ adsorption potential. Such an overestimation may occur for natural mudrocks, which commonly contain a significant amount of exchangeable $Ca^{2+}$.

## CRedit author contribution statement

Paweł P. Ziemiański and Arkadiusz Derkowski designed the study, interpreted data, and wrote the paper. Paweł P. Ziemiański performed methane high-pressure adsorption measurements. Jakub Szczurowski provided $N_2$ and $CO_2$ adsorption data; Marcin Kozieł performed XRD measurements

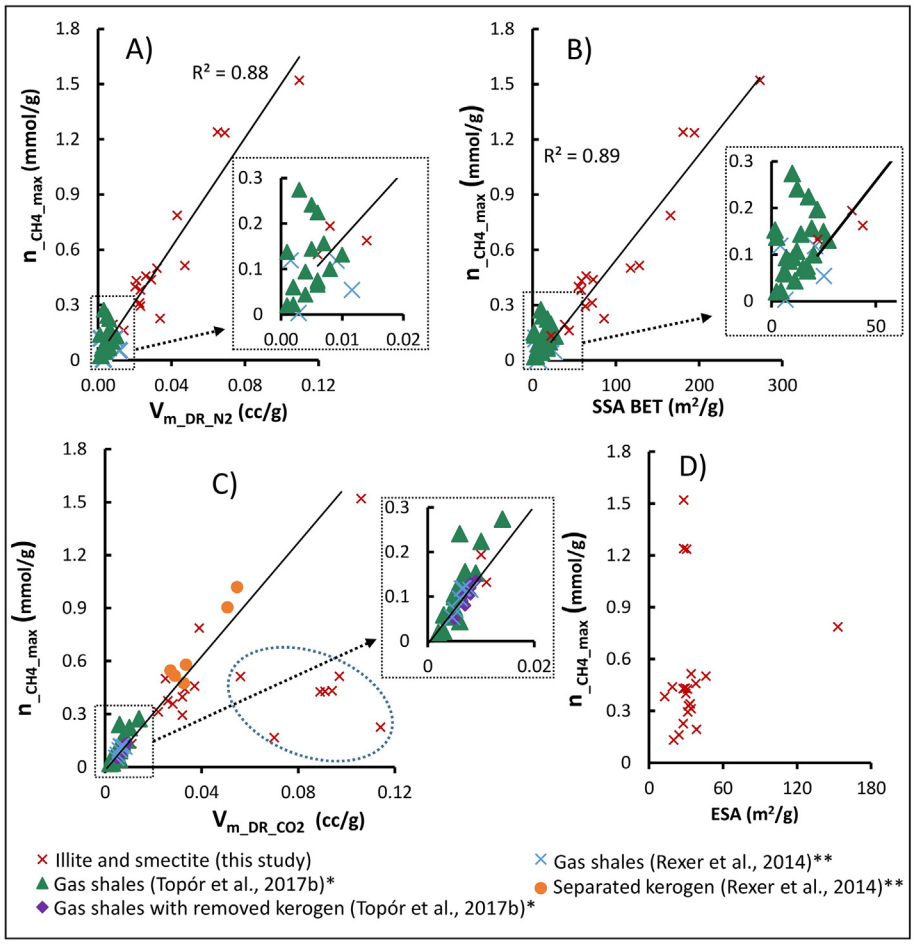


**Fig. 10.** Comparison of maximum high-pressure methane excess adsorption with $N_2$ and $CO_2$ micropore volume, specific surface area BET, and external surface area. Available data from literature obtained on unmodified and modified gas shales were included. *$N_2$–based micropore volume were not presented in original paper **$CH_4$ adsorption conducted at 45 °C.

## Declaration of Competing Interest

The authors declare that they have no known competing financial interests or personal relationships that could have appeared to influence the work reported in this paper.

## Acknowledgments

This study was financed by National Science Centre, Poland, grant no. 2017/25/N/ST10/02034. This study was completed to fulfill partially the requirements of a Ph.D. thesis by P.P. Ziemiański. We are grateful to the reviewers, Pieter Bertier and Helge Stanjek for valuable remarks and to Nadine Kanik for English language corrections.

## Appendix A. Supplementary data

Supplementary materials to this article can be found online at https://doi.org/10.1016/j.coal.2020.103483.

## References

Aylmore, L.A.G., 1974. Gas sorption in clay mineral systems. Clay Clay Miner. 22, 175–183. https://doi.org/10.1346/CCMN.1974.0220205.

Barrer, R.M., MacLeod, D.M., 1955. Activation of montmorillonite by ion exchange and sorption complexes of tetra-alkyl ammonium montmorillonites. Trans. Faraday Soc. 51, 1290. https://doi.org/10.1039/tf9555101290.

de Boer, J.H., Lippens, B.C., Linsen, B.G., Broekhoff, J.C.P., van den Heuvel, A., Osinga, T.J., 1966. Thet-curve of multimolecular $N_2$-adsorption. J. Colloid Interface Sci. 21, 405–414. https://doi.org/10.1016/0095-8522(66)90006-7.

Bowers, G.M., Schaef, H.T., Loring, J.S., Hoyt, D.W., Burton, S.D., Walter, E.D., Kirkpatrick, R.J., 2017. Role of cations in $CO_2$ adsorption, dynamics, and hydration in smectite clays under in situ supercritical $CO_2$ conditions. J. Phys. Chem. C 121, 577–592. https://doi.org/10.1021/acs.jpcc.6b11542.

Bowers, G.M., Loring, J.S., Schaef, H.T., Walter, E.D., Burton, S.D., Hoyt, D.W., Cunniff, S.S., Loganathan, N., Kirkpatrick, R.J., 2018. Interaction of hydrocarbons with clays under reservoir conditions: in situ infrared and nuclear magnetic resonance spectroscopy and X-ray diffraction for expandable clays with variably wet supercritical methane. ACS Earth Sp. Chem. 2, 640–652. https://doi.org/10.1021/acsearthspacechem.8b00039.

Brunauer, S., Emmett, P.H., Teller, E., 1938. Adsorption of gases in multimolecular layers. J. Am. Chem. Soc. 60, 309–319. https://doi.org/10.1021/ja01269a023.

Cases, J.M., Bérend, I., François, M., Uriot, J.P., Michot, L.J., Thomas, F., 1997. Mechanism of adsorption and desorption of water vapor by homoionic montmorillonite: 3. The $Mg^{2+}$, $Ca^{2+}$, $Sr^{2+}$ and $Ba^{2+}$ exchanged forms. Clay Clay Miner. 45, 8–22. https://doi.org/10.1346/CCMN.1997.0450102.

Cazorla-Amorós, D., Alcañiz-Monge, J., de la Casa-Lillo, M.A., Linares-Solano, A., 1998. $CO_2$ as an adsorptive to characterize carbon molecular sieves and activated carbons. Langmuir 14, 4589–4596. https://doi.org/10.1021/la980198p.

Chen, S.G., Yang, R.T., 1994. Theoretical basis for the potential theory adsorption isotherms. The Dubinin-Radushkevich and Dubinin-Astakhov equations. Langmuir 10, 4244–4249. https://doi.org/10.1021/la00023a054.

Cheng, A.-L., Huang, W.-L., 2004. Selective adsorption of hydrocarbon gases on clays and organic matter. Org. Geochem. 35, 413–423. https://doi.org/10.1016/j.orggeochem.2004.01.007.

Chiou, C.T., Rutherford, D.W., 1997. Effects of exchanged cation and layer charge on the sorption of water and EGME vapors on montmorillonite clays. Clay Clay Miner. 45, 867–880. https://doi.org/10.1346/CCMN.1997.0450611.

Do, D.D., Do, H.D., 2003. Adsorption of supercritical fluids in non-porous and porous carbons: analysis of adsorbed phase volume and density. Carbon 41, 1777–1791. https://doi.org/10.1016/S0008-6223(03)00152-0.

Dreisbach, F., Lösch, H.W., 2000. Magnetic suspension balance for simultaneous measurement of a sample and the density of the measuring fluid. J. Therm. Anal. Calorim. 62, 515–521. https://doi.org/10.1023/A:1010179306714.

Dreisbach, F., Lösch, H.W., Harting, P., 2002. Highest pressure adsorption equilibria data: Measurement with magnetic suspension balance and analysis with a new adsorbent/

adsorbate-volume. Adsorption 8, 95–109. https://doi.org/10.1023/A:1020431616093.
Ferrage, E., Kirk, C.A., Cressey, G., Cuadros, J., 2007a. Dehydration of Ca-montmorillonite at the crystal scale. Part I: Structure evolution. Am. Mineral. 92, 994–1006. https://doi.org/10.2138/am.2007.2396.
Ferrage, E., Kirk, C.A., Cressey, G., Cuadros, J., 2007b. Dehydration of Ca-montmorillonite at the crystal scale. Part 2. Mechanisms and kinetics. Am. Mineral. 92, 1007–1017. https://doi.org/10.2138/am.2007.2397.
Ferrage, E., Lanson, B., Michot, L.J., Robert, J.-L., 2010. Hydration properties and interlayer organization of water and ions in synthetic Na-smectite with tetrahedral layer charge. Part 1. Results from X-ray diffraction profile modeling. J. Phys. Chem. C 114, 4515–4526. https://doi.org/10.1021/jp909860p.
Fripiat, J.J., Cruz, M.I., Bohor, B.F., Thomas, J.J., 1974. Interlamellar adsorption of carbon dioxide by smectites. Clay Clay Miner. 22, 23–30. https://doi.org/10.1346/CCMN.1974.0220105.
Garrels, R.M., Mackenzie, F.T., 1971. Evolution of Sedimentary Rocks. Norton, New York.
Gasparik, M., Rexer, T.F.T., Aplin, A.C., Billemont, P., De Weireld, G., Gensterblum, Y., Henry, M., Krooss, B.M., Liu, S., Ma, X., Sakurovs, R., Song, Z., Staib, G., Thomas, K.M., Wang, S., Zhang, T., 2014. First international inter-laboratory comparison of high-pressure $CH_4$, $CO_2$ and $C_2H_6$ sorption isotherms on carbonaceous shales. Int. J. Coal Geol. 132, 131–146. https://doi.org/10.1016/j.coal.2014.07.010.
Giesting, P., Guggenheim, S., Koster van Groos, A.F., Busch, A., 2012a. Interaction of carbon dioxide with Na-exchanged montmorillonite at pressures to 640 bars: Implications for $CO_2$ sequestration. Int. J. Greenh. Gas Control 8, 73–81. https://doi.org/10.1016/j.ijggc.2012.01.011.
Giesting, P., Guggenheim, S., Koster van Groos, A.F., Busch, A., 2012b. X-ray diffraction study of K- and Ca-exchanged montmorillonites in $CO_2$ atmospheres. Environ. Sci. Technol. 46, 5623–5630. https://doi.org/10.1021/es3005865.
Guggenheim, S., Koster van Groos, A.F., 2003. New gas-hydrate phase: Synthesis and stability of clay–methane hydrate intercalate. Geology 31, 653–656. https://doi.org/10.1130/0091-7613(2003)031<0653:NGPSAS>2.0.CO;2.
Harkins, W.D., Jura, G., 1944. Surfaces of Solids. XIII. A vapor adsorption method for the determination of the area of a solid without the assumption of a molecular area, and the areas occupied by nitrogen and other molecules on the surface of a solid. J. Am. Chem. Soc. 66, 1366–1373. https://doi.org/10.1021/ja01236a048.
Heller, R., Zoback, M., 2014. Adsorption of methane and carbon dioxide on gas shale and pure mineral samples. J. Unconv. Oil Gas Resour. 8, 14–24. https://doi.org/10.1016/j.juogr.2014.06.001.
Jackson, M.L., 1969. Soil Chemical Analysis: Advanced Course, 2nd ed. Parallel Press.
Jaynes, W.F., Bigham, J.M., 1987. Charge reduction, octahedral charge, and lithium retention in heated, Li-saturated smectites. Clay Clay Miner. 35, 440–448. https://doi.org/10.1346/CCMN.1987.0350604.
Jeon, P.R., Choi, J., Yun, T.S., Lee, C.-H., 2014. Sorption equilibrium and kinetics of $CO_2$ on clay minerals from subcritical to supercritical conditions: $CO_2$ sequestration at nanoscale interfaces. Chem. Eng. J. 255, 705–715. https://doi.org/10.1016/j.cej.2014.06.090.
Ji, L., Zhang, T., Milliken, K.L., Qu, J., Zhang, X., 2012. Experimental investigation of main controls to methane adsorption in clay-rich rocks. Appl. Geochem. 27, 2533–2545. https://doi.org/10.1016/j.apgeochem.2012.08.027.
Kaufhold, S., Dohrmann, R., Klinkenberg, M., Siegesmund, S., Ufer, K., 2010. $N_2$-BET specific surface area of bentonites. J. Colloid Interface Sci. 349, 275–282. https://doi.org/10.1016/j.jcis.2010.05.018.
Kuila, U., McCarty, D.K., Derkowski, A., Fischer, T.B., Topór, T., Prasad, M., 2014. Nanoscale texture and porosity of organic matter and clay minerals in organic-rich mudrocks. Fuel 135, 359–373. https://doi.org/10.1016/j.fuel.2014.06.036.
Kuligiewicz, A., Derkowski, A., 2017. Tightly bound water in smectites. Am. Mineral. 102, 1073–1090. https://doi.org/10.2138/am-2017-5918.
Kvenvolden, K.A., 1998. A primer on the geological occurrence of gas hydrate. Geol. Soc. London. Spec. Publ. 137, 9–30. https://doi.org/10.1144/GSL.SP.1998.137.01.02.
Lee, M.-S., McGrail, B.P., Rousseau, R., Glezakou, V.-A., 2018. Molecular level investigation of $CH_4$ and $CO_2$ adsorption in hydrated calcium–montmorillonite. J. Phys. Chem. C 122, 1125–1134. https://doi.org/10.1021/acs.jpcc.7b05364.
Li, J., Li, X., Wang, X., Li, Y., Wu, K., Shi, J., Yang, L., Feng, D., Zhang, T., Yu, P., 2016. Water distribution characteristic and effect on methane adsorption capacity in shale clay. Int. J. Coal Geol. 159, 135–154. https://doi.org/10.1016/j.coal.2016.03.012.
Liang, L., Xiong, J., Liu, X., Luo, D., 2016. An investigation into the thermodynamic characteristics of methane adsorption on different clay minerals. J. Nat. Gas Sci. Eng. 33, 1046–1055. https://doi.org/10.1016/j.jngse.2016.06.024.
Lippens, B.C., Boer, J.H., 1965. Studies on pore systems in catalysts V. The t method. J. Catal. 4, 319–323. https://doi.org/10.1016/0021-9517(65)90307-6.
Liu, D., Yuan, P., Liu, H., Li, T., Tan, D., Yuan, W., He, H., 2013. High-pressure adsorption of methane on montmorillonite, kaolinite and illite. Appl. Clay Sci. 85, 25–30. https://doi.org/10.1016/j.clay.2013.09.009.
Liu, L., Nicholson, D., Bhatia, S.K., 2015. Adsorption of $CH_4$ and $CH_4/CO_2$ mixtures in carbon nanotubes and disordered carbons: a molecular simulation study. Chem. Eng. Sci. 121, 268–278. https://doi.org/10.1016/j.ces.2014.07.041.
Loganathan, N., Bowers, G.M., Yazaydin, A.O., Schaef, H.T., Loring, J.S., Kalinichev, A.G., Kirkpatrick, R.J., 2018. Clay swelling in dry supercritical carbon dioxide: effects of interlayer cations on the structure, dynamics, and energetics of $CO_2$ intercalation probed by XRD, NMR, and GCMD simulations. J. Phys. Chem. C 122, 4391–4402. https://doi.org/10.1021/acs.jpcc.7b12270.
Lowell, S., Shields, J.E., Thomas, M.A., Thommes, M., 2004. Characterization of porous solids and powders: surface area, pore size and density, characterization of porous solids and powders: surface area, pore size and density, particle technology series. Springer Netherlands, Dordrecht. https://doi.org/10.1007/978-1-4020-2303-3.
Michot, L.J., Villiéras, F., 2006. Surface area and porosity. In: Bergaya, F., Theng, B.K.G., Lagaly, G. (Eds.), Developments in Clay Science, pp. 965–978. https://doi.org/10.1016/S1572-4352(05)01035-4.
Munusamy, K., Somani, R.S., Bajaj, H.C., 2011. Tamarind seeds carbon: preparation and methane uptake. BioResources 6, 537–551.
Norrish, K., 1954. The swelling of montmorillonite. Discuss. Faraday Soc. 18, 120. https://doi.org/10.1039/df9541800120.
Post, J.L., Cupp, B.L., Madsen, F.T., 1997. Beidellite and associated clays from the DeLamar mine and Florida Mountain Area, Idaho. Clay Clay Miner. 45, 240–250. https://doi.org/10.1346/CCMN.1997.0450212.
Rajec, P., Šucha, V., Eberl, D.D., Środoń, J., Elsass, F.E., 1999. Effect of illite particle shape on cesium sorption. Clay Clay Miner. 47, 755–760. https://doi.org/10.1346/CCMN.1999.0470610.
Rao, Q., Leng, Y., 2014. Methane aqueous fluids in montmorillonite clay interlayer under near-surface geological conditions: a Grand Canonical Monte Carlo and Molecular Dynamics simulation study. J. Phys. Chem. B 118, 10956–10965. https://doi.org/10.1021/jp507884w.
Rao, Q., Xiang, Y., Leng, Y., 2013. Molecular simulations on the structure and dynamics of water–methane fluids between Na-montmorillonite clay surfaces at elevated temperature and pressure. J. Phys. Chem. C 117, 14061–14069. https://doi.org/10.1021/jp403349p.
Rexer, T.F.T., Benham, M.J., Aplin, A.C., Thomas, K.M., 2013. Methane adsorption on shale under simulated geological temperature and pressure conditions. Energy Fuel 27, 3099–3109. https://doi.org/10.1021/ef400381v.
Rexer, T.F., Mathia, E.J., Aplin, A.C., Thomas, K.M., 2014. High-pressure methane adsorption and characterization of pores in Posidonia shales and isolated kerogens. Energy Fuel 28, 2886–2901. https://doi.org/10.1021/ef402466m.
Romanov, V.N., 2013. Evidence of irreversible $CO_2$ intercalation in montmorillonite. Int. J. Greenh. Gas Control 14, 220–226. https://doi.org/10.1016/j.ijggc.2013.01.022.
Ross, D.J.K., Bustin, R.M., 2009. The importance of shale composition and pore structure upon gas storage potential of shale gas reservoirs. Mar. Pet. Geol. 26, 916–927. https://doi.org/10.1016/j.marpetgeo.2008.06.004.
Rouquerol, J., Llewellyn, P., Rouquerol, F., 2007. Is the BET equation applicable to microporous adsorbents? Stud. Surf. Sci. Catal. 160, 49–56. https://doi.org/10.1016/S0167-2991(07)80008-5.
Rutherford, D.W., Chiou, C.T., Eberl, D.D., 1997. Effects of exchanged cation on the microporosity of montmorillonite. Clay Clay Miner. 45, 534–543. https://doi.org/10.1346/CCMN.1997.0450405.
Schneider, C.A., Rasband, W.S., Eliceiri, K.W., 2012. NIH Image to ImageJ: 25 years of image analysis. Nat. Methods 9, 671–675. https://doi.org/10.1038/nmeth.2089.
Środoń, J., Zeelmaekers, E., Derkowski, A., 2009. The charge of component layers of illite-smectite in bentonites and the nature of end-member illite. Clay Clay Miner. 57, 649–671. https://doi.org/10.1346/CCMN.2009.0570511.
Steudel, A., Emmerich, K., 2013. Strategies for the successful preparation of homoionic smectites. Appl. Clay Sci. 75-76, 13–21. https://doi.org/10.1016/j.clay.2013.03.002.
Thommes, M., Kaneko, K., Neimark, A.V., Olivier, J.P., Rodriguez-Reinoso, F., Rouquerol, J., Sing, K.S.W., 2015. Physisorption of gases, with special reference to the evaluation of surface area and pore size distribution (IUPAC Technical Report). Pure Appl. Chem. 87, 1051–1069. https://doi.org/10.1515/pac-2014-1117.
Topór, T., Derkowski, A., Ziemiański, P., Marynowski, L., McCarty, D.K., 2017a. Multivariable constraints of gas exploration potential in the Lower Silurian shale of the Baltic Basin (Poland). Int. J. Coal Geol. 179, 45–59. https://doi.org/10.1016/j.coal.2017.05.001.
Topór, T., Derkowski, A., Ziemiański, P., Szczurowski, J., McCarty, D.K., 2017b. The effect of organic matter maturation and porosity evolution on methane storage potential in the Baltic Basin (Poland) shale-gas reservoir. Int. J. Coal Geol. 180, 46–56. https://doi.org/10.1016/j.coal.2017.07.005.
Veblen, D.R., Guthrie, G.D.J., Livi, K.J.T., Reynolds, R.C.J., 1990. High-resolution transmission electron microscopy and electron diffraction of mixed-layer illite/smectite: experimental results. Clay Clay Miner. 38, 1–13. https://doi.org/10.1346/CCMN.1990.0380101.
Viczián, I., 1997. Hungarian investigations on the “Zempleni” illite. Clay Clay Miner. 45, 114–115. https://doi.org/10.1346/CCMN.1997.0450114.
Whitley, H.D., Smith, D.E., 2004. Free energy, energy, and entropy of swelling in Cs–, Na–, and Sr–montmorillonite clays. J. Chem. Phys. 120, 5387–5395. https://doi.org/10.1063/1.1648013.
Wilson, M.J., Shaldybin, M.V., Wilson, L., 2016. Clay mineralogy and unconventional hydrocarbon shale reservoirs in the USA. I. Occurrence and interpretation of mixed-layer R3 ordered illite/smectite. Earth Sci. Rev. 158, 31–50. https://doi.org/10.1016/j.earscirev.2016.04.004.
Zee Ma, Y., 2016. Unconventional resources from exploration to production. In: Unconventional Oil and Gas Resources Handbook. Elsevier, pp. 3–52. https://doi.org/10.1016/B978-0-12-802238-2.00001-8.